JGR Atmospheres

RESEARCH ARTICLE
10.1029/2021JD035149

Investigations on Concentric Gravity Wave Sources Over the Brazilian Equatorial Region

P. K. Nyassor[1], C. M. Wrasse[1], I. Paulino[2], D. Gobbi[1], E. Yiğit[3], H. Takahashi[1], P. P. Batista[4], K. P. Naccarato[5], R. A. Buriti[2], A. R. Paulino[6], D. Barros[1], and C. A. O. B. Figueiredo[1]

[1]Space Weather Division, National Institute for Space Research, São José dos Campos, Brazil, [2]Department of Physics, Federal University of Campina Grande, Campina Grande, Brazil, [3]Department of Physics and Astronomy, George Mason University, Fairfax, VA, USA, [4]Heliophysics, Planetary Science and Aeronomy Division, National Institute for Space Research, São José dos Campos, Brazil, [5]Impacts, Adaptation and Vulnerabilities Division, National Institute for Space Research, São José dos Campos, Brazil, [6]Department of Physics, Paraíba State University, Campina Grande, Brazil

Key Points:

- Concentric gravity waves over the Brazilian equatorial region are presented
- The concentric wavefront configurations were examined relative to their propagation from the observation to the source positions
- The unknown source of one of the concentric GWs without a nearby deep convective system is investigated

Supporting Information:

Supporting Information may be found in the online version of this article.

Correspondence to:

P. K. Nyassor,
prosper.nyassor@inpe.br

Citation:

Nyassor, P. K., Wrasse, C. M., Paulino, I., Gobbi, D., Yiğit, E., Takahashi, H., et al. (2022). Investigations on concentric gravity wave sources over the Brazilian equatorial region. *Journal of Geophysical Research: Atmospheres*, *127*, e2021JD035149. https://doi.org/10.1029/2021JD035149

Received 26 APR 2021
Accepted 10 AUG 2022

Author Contributions:

Conceptualization: P. K. Nyassor, C. M. Wrasse, I. Paulino, E. Yiğit, C. A. O. B. Figueiredo
Formal analysis: P. K. Nyassor
Funding acquisition: C. M. Wrasse
Methodology: P. K. Nyassor, C. M. Wrasse, D. Gobbi, K. P. Naccarato, R. A. Buriti, A. R. Paulino, D. Barros, C. A. O. B. Figueiredo
Software: P. K. Nyassor, C. M. Wrasse, I. Paulino, K. P. Naccarato, R. A. Buriti, A. R. Paulino, D. Barros, C. A. O. B. Figueiredo
Supervision: C. M. Wrasse, I. Paulino, D. Gobbi
Validation: P. K. Nyassor, C. M. Wrasse, I. Paulino, D. Gobbi, E. Yiğit, H. Takahashi, K. P. Naccarato, R. A. Buriti, D. Barros, C. A. O. B. Figueiredo
Writing – original draft: P. K. Nyassor

Abstract Observations of concentric gravity waves (CGWs) in the OH airglow emission over the Brazilian equatorial region are presented. An all-sky imager installed at São João do Cariri [7.4°S, 36.5°W] was used to acquire near-infrared OH images. Using over 19 years of observational data from 2000 to 2019, more than 1,052 clear sky nights of airglow data were acquired with a total of 25 observed CGW cases. Three CGW events were selected for this study. These waves had small-scale characteristics and well-defined concentric structures. The selected CGW events showed horizontal wavelengths $\lambda_H \sim$ 31.9, 42.5, and 30.9 km, horizontal phase speeds $c_H \sim$ 49.2, 57.6, and 74.1 m/s, and periods $\tau \sim$ 10.8, 12.3, and 7.0 min, respectively. The CGW structures were well defined, with coherent wave patterns expanding concentrically from the source point, with the observed events having semi-circle or arc-like and semi-elliptical shapes. We found the occurrence of the CGWs to coincide with the seasons of intense tropospheric convective activity and low background winds. This suggests little or no wave breaking, critical level absorption, and filtering or reflection, thereby allowing the CGWs to propagate up to the mesosphere and lower thermosphere region. Using backward ray tracing, we also found the positions and times where and when the ray paths reached the tropopause. The tropopause positions and times of two of the CGW events coincide with active convective systems with cold cloud top temperatures. However, the tropopause position of one of the 3 CGW events did not coincide with any active convective system, suggesting that this CGW was most likely generated in-situ.

Plain Language Summary Point-like convective overshooting of the tropopause by 1–3 km into the stratosphere can excite GWs with concentric shapes. These waves can propagate to the middle and upper atmosphere where they are observed using imaging techniques. Also, some GWs with concentric shapes are excited when GWs primarily generated in the lower atmosphere dissipate or break. To study the propagation of these concentric gravity waves (CGWs) in the atmosphere from the observation altitudes to their possible source locations in the troposphere, the ray tracing model was used. The ray tracing results revealed that the state and impact of the background winds on the propagation of the CGWs differ for each of the three cases presented. Among the three CGWs, it was evident that the event with relatively strong and variable wind, the vertical, horizontal, and temporal propagations were significantly affected. The stopping points of the ray paths of the waves used to locate the possible source positions of the CGWs showed that the ray paths of two out of the three CGW cases stopped near deep convective systems in the troposphere, indicating these systems are their possible source. The ray path of the remaining CGW case stopped in the troposphere but no deep convective system was found close to the stopping point, thus suggesting this wave was not convectively generated.

1. Introduction

The dynamics of atmospheric gravity waves (AGWs/GWs) dominate several altitudes throughout the atmosphere due to its diverse effects on the physical processes and global circulation system (Yiğit & Medvedev, 2015). GWs transfer momentum and energy upward from the regions of their primary sources in the lower atmosphere to the upper layers of the atmosphere, where they deposit the transported momentum and energy by various dissipative

Writing – review & editing: C. M. Wrasse, I. Paulino, D. Gobbi, E. Yiğit, H. Takahashi, P. P. Batista, K. P. Naccarato, R. A. Buriti, A. R. Paulino, D. Barros, C. A. O. B. Figueiredo

mechanisms (Fritts & Alexander, 2003). The altitude of wave dissipation depends on the conditions of the background atmosphere through which it propagates (e.g., Tsuda, 2014).

According to Nappo (2013), atmospheric waves cannot exist without a source in appropriate stability and dynamic conditions. Latent heat release in convective fronts, overshooting of tropopause by thunderstorms, and orographic forcing are noted to be the dominant GW excitation mechanisms in the troposphere (Fritts et al., 2006). Beyond the tropopause, the most effective mechanisms responsible for GW generation are wind shear, spontaneous adjustment, and body forcing (Fritts et al., 2006; Vadas et al., 2018). Efforts by various authors via observational results (e.g., Vadas & Liu, 2009; Yue et al., 2009, 2013) and simulations (e.g., Lane et al., 2001, 2003; Vadas, 2007; Yiğit et al., 2021) have striven in explaining and relating waves generated in the troposphere and beyond to the observed waves in the upper atmosphere. These studies gave a further understanding of the impact of propagating waves on the middle atmosphere circulation and temperature structures (Vargas et al., 2016; Wrasse et al., 2003).

Observations of GWs in the mesosphere and lower thermosphere (MLT) region are made using airglow all-sky cameras (e.g., Nyassor et al., 2018; Paulino et al., 2020), and Middle and Upper atmosphere radars (e.g., Tsuda, 2014). These observational techniques allow measurement of the spatial and temporal characteristics of the GW perturbations instantaneously (e.g., Bageston et al., 2009). Wave perturbations with large vertical wavelength, phase speed, and high-frequency are more readily observed in airglow imagery (e.g., Liu & Swenson, 2003) due to vertical transportation of horizontal momentum flux (Vargas et al., 2016). One significant effect of high-frequency waves breaking is the triggering of a broad spectrum of secondary GWs whose frequencies depend on the duration of the body forces which are of order or larger than the primary wave period (Vadas & Fritts, 2001).

GWs with distinct shapes have been observed in the upper atmosphere in nightglow images, among which planar GWs are the most frequently seen (Yue et al., 2009). Even though the sources of CGWs and their propagation in the atmosphere have a peculiar nature, some GWs with concentric wavefronts have been reported in literature (e.g., Nyassor et al., 2021; Sentman et al., 2003; Suzuki et al., 2007, 2013; Vadas et al., 2012; Xu et al., 2015; Yue et al., 2009, 2013). A satellite-based climatological study conducted by Perwitasari et al. (2016) showed a relatively higher number of GWs with concentric structures than the ones detected by ground-based studies. This is because the field of view of ground-based observational systems (e.g., all-sky imagers) are mostly obstructed by the very convective systems that excite concentric gravity waves (CGWs) (Akiya et al., 2014; Yue et al., 2009).

The knowledge of the sources of the observed waves is a key factor to be considered since it aides the understandability of the wave characteristics in relation to their sources. The ray tracing numerical technique is widely used in identifying the likely source positions of waves observed in the MLT region based on the influence of the background wind and temperature relative to the wave trajectory. The general principle of this technique was discussed by Lighthill (1978), after which several improvements were implemented by other researchers (e.g., Eckermann, 1992; Paulino et al., 2012; Vadas, 2007; Vadas & Fritts, 2005; Wrasse et al., 2003) in order to study the wave propagation in a more realistic atmosphere. The sources of primary CGWs are related to convective overshooting of the tropopause. The overshooting is mainly observed in the infrared cloud top brightness temperature (CTBT) imagery.

On the other hand, the generation mechanism of CGWs explained in the works by Vadas et al. (2003, 2018) showed that secondary GWs excited by horizontal body force during the breaking of primary waves also have concentric structures. In such cases, further investigation is needed to find the exact location of the source. Kogure et al. (2020) reported the first observational result of secondary GWs using multiple altitude satellite observations of breaking mountain waves over the Andes. Their work complemented the theoretical basis proposed by Vadas and Becker (2019). Also, numerous simulation studies (e.g., Heale et al., 2019, 2020; Lane et al., 2001, 2003) have extensively studied the generation, propagation, and dissipation of both convective and non-convective GWs. Heale et al. (2019, 2020) explained using simulation to study the generation, propagation, dissipation or breaking of convective GWs and mountain waves, respectively. They further demonstrated that the spectrum of non-primary GWs were excited as a result of the breaking convective GWs and mountain waves.

Global distribution studies, using 3 years of CGWs data conducted by Perwitasari et al. (2016) showed high occurrence in midlatitudes and low occurrence in the equatorial regions. In the Brazilian equatorial region, strong GW activities have been reported using ground-based instruments (e.g., Paulino et al., 2020, and refer-

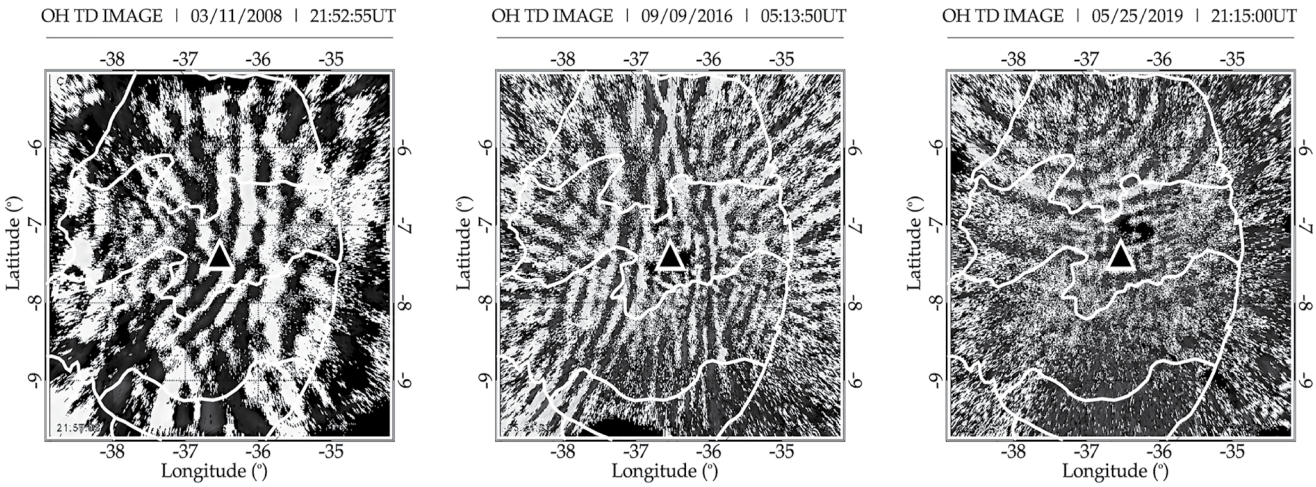

Figure 1. Samples of unwarped, time-difference (TD) images of each concentric gravity wave events observed over São João do Cariri are presented. The left panel is the event of 11 March 2008, in the middle is the event of 9 September 2016, and in the right panel, the event of 25 May 2019 is presented. The black triangle with white outline shows the center of the image (indicating the São João do Cariri observatory). The white lines show the borders of Brazilian states.

ences therein). However, convective activity during some seasons of the year is high, making it possible for the occurrence of CGWs. In this current work, we will present case studies of three CGW events observed over the Brazilian equatorial region. Each of the events has a distinct characteristic relative to the source. Using a ray tracing model, the source locations of two CGW events were identified to be associated with deep tropospheric convection, whereas, one out of the three showed otherwise. Further analysis on the propagation characteristics showed that this CGW (without nearby convective system) could not be generated directly by the convective systems more than 1,000 km west of the observation site. For the first time, ground-based observation of CGWs without direct association with deep convection in the Brazilian equatorial region has been reported.

2. Gravity Wave Characteristics

A high-sensitive all-sky imager with an effective field of view of about 145° operated at the São João do Cariri (7.4°S, 36.5°W) observatory was used in the airglow observations. Images of OH, OI557.7, and OI630.0 nm emission layers were acquired, but only OH airglow images were used in this study. A detailed description of the imager and the required image acquisition modes can be found in previous studies (Medeiros et al., 2005; Nyassor et al., 2018; Paulino et al., 2020).

To visualize concentric GWs patterns in OH airglow images, the original images were first preprocessed. The preprocessing involves; the alignment of the image to the correct geographic north, removal of stars, and the linearization of the image, that is, the removal of the curvature effect of the objective lens by projecting the image onto the horizontal plane. More information on the preprocessing can be found in the work by Garcia et al. (1997) and Wrasse et al. (2007). Out of ∼19 years of OH airglow observation using an all-sky imager from 2000 to 2019, of which we have more than 1,052 nights with clear sky conditions, three (3) CGW cases out of a total of 25 CGWs detected cases were chosen for this study. For the CGW cases considered for this study, the following criteria were used: (a) the shape of the concentric wavefront and (b) the proximity of convective sources. Figure 1 shows an unwarped (linearized), time-difference (TD) image of the selected cases for this study.

In order to obtain the CGWs horizontal parameters (e.g., wavelength (λ_H), period (τ), phase speed (c_H), and propagation direction(ϕ)), spectral analysis technique was used (e.g., Garcia et al., 1997; Wrasse et al., 2007). To determine GW parameters from all-sky images, the original airglow images are first preprocessed. In preprocessing, the original airglow images with temporal resolution of 1.4 min were calibrated (i.e., aligned to the geographical north), the stars were removed, then unwarped, and finally mapped onto the geographical coordinates (Nyassor et al., 2021). To apply spectral analysis to the preprocessed images, regions of interest (ROI), that is, regions with visible waves (clear dark and bright bands) were then selected after which, a time series of 10 images was constructed. A two-dimensional discrete Fourier transform (2D-DFT) was then applied to the ROI in

Table 1
Concentric Gravity Waves Parameters Observed at São João do Cariri

Wave parameters	03/11/2008	09/09/2016	05/25/2019
λ_H (km)	31.9	42.5	30.9
ϕ (°)	86.4	85.2	160.6
c_H (m/s)	49.2	57.6	74.1
τ (min)	10.8	12.3	7.0
Radius (km)	200.0	460.0	Major: 150.0
			Minor: 90.0

the selected time series images. The amplitude and the phase obtained from the cross-spectrum of the 2D-DFT were used to estimate the wavelength (λ_H), period (τ), phase speed (c_H), and propagation direction (ϕ). More information on the spectral analysis can be found in Wrasse et al. (2007), Bageston et al. (2011), Giongo et al. (2020), and Nyassor et al. (2021). Gravity wave parameters of the three selected CGW events are summarized in Table 1.

3. Ray Tracing Technique

The possible source locations of the observed CGWs were estimated using the numerical ray tracing model. The model used is based on the approach that incorporates the kinematic viscosity and thermal diffusivity (Paulino et al., 2012; Vadas, 2007; Vadas & Fritts, 2005), which considers the damping effect of high-frequency GW in the thermosphere-ionosphere altitude. To estimate the next step in space and time, the equations

$$\frac{dx_i}{dt} = V_i + \frac{\partial \omega_{Ir}}{\partial k_i} = V_i + c_{g_i} \tag{1}$$

and

$$\frac{dk_i}{dt} = -k_j \frac{\partial V_j}{\partial x_i} - \frac{\partial \omega_{Ir}}{\partial x_i} \tag{2}$$

were solved numerically using the Runge-Kutta method (Press et al., 2007). The indices $i, j = 1, 2, 3$ denote the components of vector quantities: position ($\vec{x}$), background wind velocity ($\vec{V}$), wavenumber ($\vec{k}$), and the group velocity $\vec{c_g}$. ω_{Ir} is the intrinsic frequency of the wave and is defined as $\omega_{Ir} = \omega_r - kU - lV$ with ω_r being the real part of the ground-based frequency ω. The intrinsic frequency is determined at any location because ω_r remains constant along the propagation path provided the unperturbed background variables are time independent (Lighthill, 1978; Vadas & Fritts, 2005). The initial position ($\vec{x}$) where the ray tracing began was the location of the first visible concentric crest or trough in the OH emission layer altitude, that is, $x_0 = (lon_0; lat_0; alt_0)$.

The wave parameters, background wind, and temperature were considered to investigate the propagation of waves relative to the background atmosphere from the observation altitude to the possible generation region. For this study, the wind data from the Modern-Era Retrospective analysis for Research and Applications, Version 2 (MERRA-2) (Gelaro et al., 2017) and Horizontal Wind Model 2014 Version (HWM14) (Drob et al., 2015) and temperature from MERRA-2 and Mass-Spectrometer-Incoherent-Scatter (NRLMSISE-00) (e.g., Picone et al., 2002) were used. Since the altitude range of MERRA-2 wind and temperature is limited up to 75 km, MERRA-2 and HWM14 wind data and MERRA-2 and NRLMSISE-00 temperature data were concatenated to attain the required altitude range from the ground up to 100 km. Also, meteor radar winds and SABER temperature were used when data is available. The initial wave vectors (k, l, m) were obtained from the horizontal component (k, l) using $\lambda_H = 2\pi/k_H = 2\pi/\sqrt{k^2 + l^2}$ and from Equation 5 of Vadas (2007), the vertical component (m) was obtained. During the iteration, adapted stopping conditions from Paulino et al. (2012) were imposed based on some propagation characteristics relative to the background atmosphere. These stopping conditions are:

1. The group velocity should be less than or equal to 0.9 times the speed of sound ($c_g \leq 0.9Cs$)
2. The real component of the intrinsic frequency must be greater than zero ($\omega_{Ir} > 0$)
3. The momentum flux at all points of the wave trajectory must satisfy the expression: $R_m > 10^{-15} R_0$, where R_m is the momentum flux at each altitude and R_0 is the momentum flux at the reference altitude. The factor 10^{-15} was arbitrarily chosen
4. The module of the vertical wavelength must be less than viscosity scale $\left[|\lambda_z| < \frac{2\pi}{\frac{d\nu/dz}{\nu}}\right]$, where $\nu = \frac{\mu}{\rho}$ is kinematic viscosity, μ is molecular viscosity and ρ is density. The value of ν varies with altitude according to $\mu = 3.34 \times 10^{-4}\, T^{0.71}$, with T being temperature (Vadas, 2007).

Violation of any of the conditions, the process is interrupted and ended. More details on the stopping conditions can be found in Paulino et al. (2012) and Vadas (2007).

Besides using the backward ray tracing to identify the possible source position of the observed waves, the center of the concentric wavefront was also used. Knowing the center, which is determined assuming zero wind, the position of the center should be close to the tropopause position of the zero wind ray path. If the observed or modeled wind is weak (i.e., <30 m/s), the tropopause position of both zero and model winds ray paths should be close to the determined center. The center of the concentric wavefronts was determined employing a geometric approach of Pedoe (1995) using the interception of three equal intersecting circles. Three circles with arbitrary centers are drawn on the first visible concentric wavefront such that every two adjacent circles intersect. The intersecting point of the two intersecting adjacent circles is the center. The radius was estimated by constructing a right-angle triangle using the intersecting lines and a line joining any of the two centers of the three circles on the concentric wave crest (Nyassor et al., 2021).

In the case of the semi-elliptical wavefronts, three (3) positions were selected on the first visible wavefront, one at the vertex and two at the respective co-vertex. Since ellipse has two axes, that is, major axis and minor axis, arbitrary axes pairs were selected. Knowing the positions of the vertex and co-vertex on the wavefront and the pair of axes, a series of complete elliptical shapes were geometrically constructed until the best axes pairs that best fit the semi-elliptical wavefront. The center of the ellipse is the intersection point of the major and minor axis.

4. Results

The three selected CGWs observed in São João do Cariri were reverse ray traced using concatenated MERRA-2 and HWM14 model wind as background fields. Comparisons of the zero wind (not shown) and model winds ray tracing results and the geometrically determined CGW centers enable the investigation of the wind effect on the GWs ray path. The zero wind ray path and the determined center give the zeroth-order approximation of the source position.

Figure 2 shows the horizontal backward ray paths along longitude and latitude for the model wind, their temporal variation with altitude, and vertical wind profiles. For each panel, the triangle represents the location of the observation site. The plus symbol denotes the position of the first crest where the ray tracing began. The blue solid lines represent the model wind's ray paths of the waves. The blue filled circles denote where and when the GWs ray paths stopped. The diamond symbol represents the centers of the concentric structures, that is, the red dashed circles and ellipse. The asterisks in the left and middle panels represent the tropopause altitudes. High frequency CGWs are known to be generated by overshooting of the tropopause by strong updrafts during thunderstorms (Alexander et al., 1995; Azeem et al., 2015; Nyassor et al., 2021; Vadas, Taylor, et al., 2009; Xu et al., 2015; Yue et al., 2009); hence, the CTBT images corresponding to the position and time when the ray path of the waves reached the tropopause were over-plotted together with the ray paths in panels (i) of Figure 2. The brightness temperature scale of the CTBT images is defined by the colorbar.

Among the three (3) CGW events presented, two (2) of the ray paths of the two of the events (i.e., 11 March 2008 and 25 May 2019) tropopause or stopping positions were close to nearby active convective systems. However, in the case of the 9 September 2016 event, the tropopause and stopping positions of the ray path were far from the center of the first visible concentric wavefront. Also, no convective system was available at the time the ray path reached the tropopause. CTBT infrared images from Geostationary Operational Environmental Satellite (GOES) were used to study the convective activity at the tropopause. The coldest regions of the cloud top (which indicate overshooting) were used in identifying the likely sources of the observed waves. Prior to the formation of deep convection from which CTBT information is inferred, convective available potential energy (CAPE) is mostly used as an indicator (Holton, 1992). This possibility was verified using CAPE maps corresponding to the hour within which each of the waves was excited. Also, daily precipitation during the CGW events was used to further prove the existence of systems. In Figure 3, the CAPE maps and daily precipitation are presented.

The CAPE maps were used to provide information on the stability of the troposphere during the CGW events. CAPE gives a measure of the quantity of energy available for convection and it is directly related to the maximum updraft velocity; thus higher values indicate a greater possibility of severe weather (Holton, 1992). The CAPE data used for the CAPE map in panels (a(i)), (b(i)), and (c(i)) of Figure 3 was obtained from the European Centre for

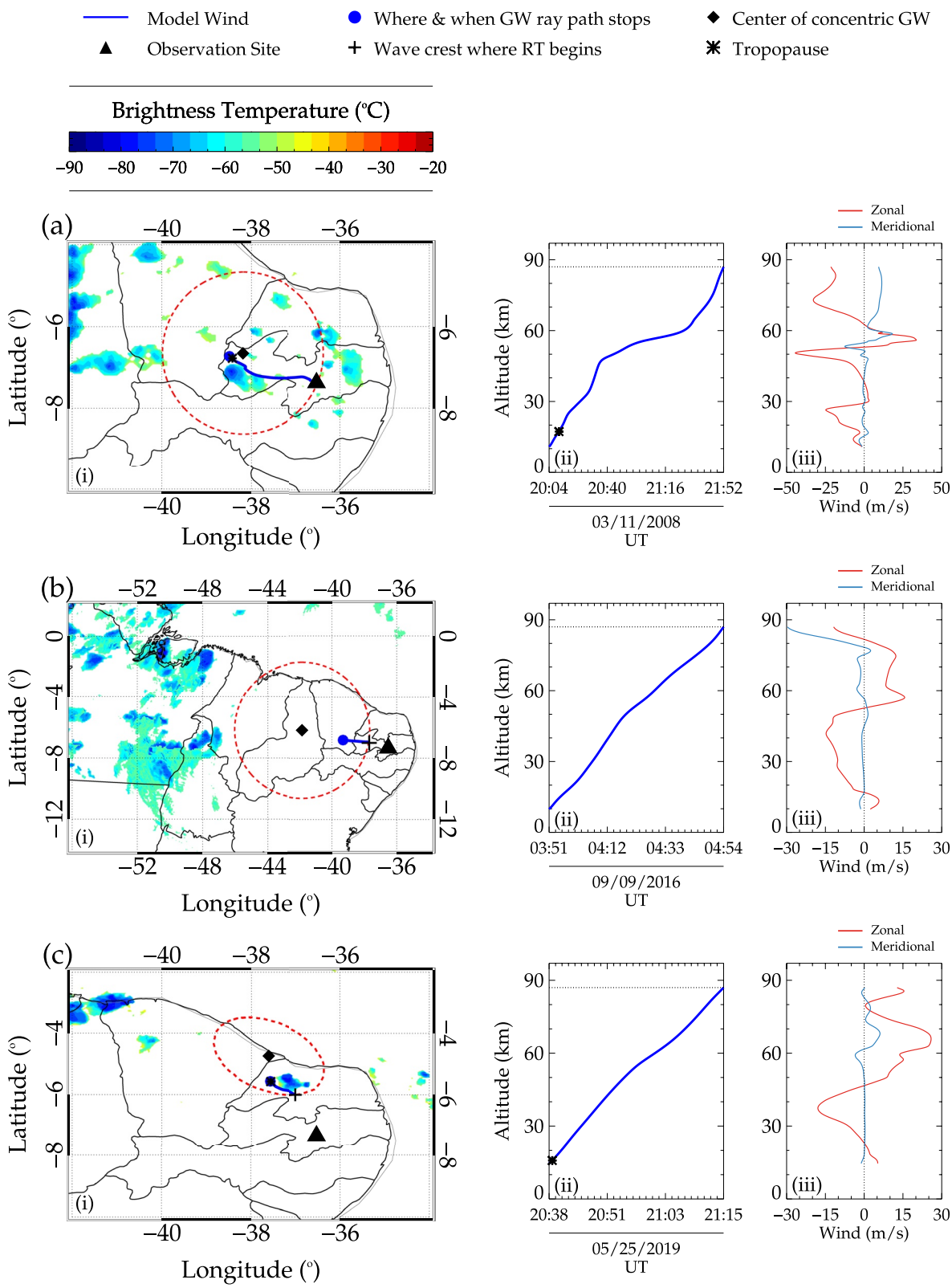
Model Wind
Where & when GW ray path stops
Center of concentric GW
Observation Site
Wave crest where RT begins
Tropopause
Brightness Temperature (°C)
−90 −80 −70 −60 −50 −40 −30 −20
(a)
(b)
(c)
(i)
(ii)
(iii)
Latitude (°)
Longitude (°)
Altitude (km)
Zonal
Meridional
Wind (m/s)
03/11/2008
UT
09/09/2016
UT
05/25/2019
UT

Figure 2.

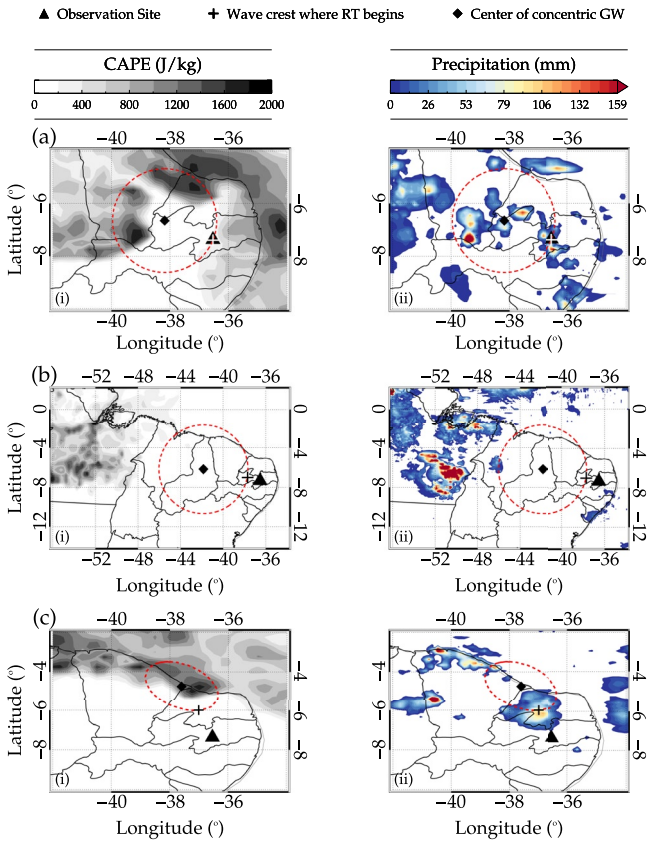

Figure 3. Convective available potential energy (CAPE) and daily precipitation during the three concentric gravity wave (CGW) events at São João do Cariri. In panels (a(i)), (b(i)), and (c(i)), the CAPE maps of the hour within which each of the CGWs were excited are shown whereas, in panels (a(ii)), (b(ii)), and (c(ii)), the daily precipitation are presented. The black triangle, diamond, and plus symbol shows the observation site, center of the concentric wavefront, and the position where the ray tracing began, respectively. The red dashed circles and ellipse show the first visible concentric structures in the OH images for each event.

Medium-Range Weather Forecasts (ECMWF) Reanalysis version 5 [ERA5]. Details on how to access the data can be found in Hersbach et al. (2018).

The occurrence of deep convection with active minimum cloud top brightness temperatures corresponding to the time when the ray path reached the tropopause has been used by Dare-Idowu et al. (2020) to identify convection and potential sources of GWs. As presented in Figure 2, the concentric wavefronts of 11 March 2008 and 9 September 2016 CGW events were arc-like whereas that of 25 May 2019 event was semi-elliptical. Except for 9 September 2016 CGW event, the tropopause or stopping positions of 11 March 2008, and 25 May 2019 were located near convective sources. The same first visible concentric wavefronts on the first OH image with concentric structures depicted by the red-dashed circles and the ellipse in Figure 2 are overlaid on the CAPE and daily precipitation maps in Figure 3, as well. The CAPE maps at the determined times of wave excitation estimated by the ray tracing model and daily precipitation for each CGW event shown in panels (a), (b), and (c) in Figure 2 is presented in panels (a), (b), and (c) in Figure 3, respectively.

To study the state of the troposphere in relation to the deep convection (the possible source of CGWs), the CAPE was considered. The CAPE maps showed high values close to the vicinity of the tropopause or stopping positions of the ray paths of the 11 March 2008 and 25 May 2019 CGWs events in panels (a(i)) and (c(i)) of Figure 3. The CAPE maps between 18:00 UT–23:00 UT for these two events, ranges between 1,000 and 2,000 J/kg. On the other hand, the CAPE maps showed low values in the vicinity of the center and also the stopping position of the ray paths of the 9 September 2016 CGW event. To define the stability and instability condition of the troposphere, we adapted the definition of the Storm Prediction Center of the National Oceanic and Atmospheric Administration (NOAA). According to their definition, values of CAPE <1,000 J/kg are defined as weak instability, 1,000 J/kg < CAPE <2,500 J/kg as moderate instability, 2,500 J/kg < CAPE <4,000 J/kg as strong instability, and CAPE >4,000 J/kg as extreme instability (NOAA, 2019). Note that these definitions are dependent on location and time of year.

To follow the CAPE activities before, during, and after the three CGW events, a six-hour CAPE map at each hour including the hour within which the waves were excited was used. Figures S1–S3 in the Supporting Information S1 show the one-hour resolution CAPE maps for the nights of 11 March 2008, 9 September 2016 and 25 May 2019, respectively. The maximum updraft velocities (w) (Holton, 1992) determined from the CAPE ranged from 44.72 to 63.25 m/s for the events of 11 March 2008 and 25 May 2019 near the center or tropopause and stopping positions of their respective ray paths. The maximum w for the 9 September 2016 event, on the other hand, was less than 40 m/s centered around 42°W; 2°S, which is ~450 km from the determined center of the CGWs. These maximum updraft velocities were estimated using the relation:

$$w \sim \sqrt{2CAPE}. \tag{3}$$

Figure 2. Backward ray tracing (RT) results of the three selected concentric gravity wave (CGW) events observed at São João do Cariri. CGW events on 11 March 2008, 9 September 2016, and 25 May 2019, are presented in panels a, b, and c, respectively. In panels (a(i)), (b(i)), and (c(i)), the ray path over the map for model wind conditions are presented. The cloud top brightness temperature (CTBT) images from GOES are overplotted together with the ray path. The temperature scale of the CTBT images is defined by the colorbar. The temporal variation of the wind model ray paths with altitude are shown in panels (a(ii)), (b(ii)), and (c(ii)). In panels (a(iii)), (b(iii)), and (c(iii)), the vertical profile of the zonal (light red solid line) and meridional (light blue solid line) winds are presented. The black triangle represents the location of the observation site. The blue solid lines depict the ray path of model winds. The blue filled circles at the end of the blue solid lines show the stopping position of the ray paths, whereas the black asterisk shows the position and time where and when the ray path reached the tropopause. The black diamond shows the center of the concentric wavefront, and the black plus symbol shows the position where the ray tracing began. The red dashed circles and ellipse show the first visible concentric structures in the OH images for each event.

Reported CGWs events by Vadas, Taylor, et al. (2009) and Xu et al. (2015), showed high CAPE (updraft) either before or during the time of the wave event. During the CGW event on the night of 1 October 2005 reported by Vadas and Liu (2009), a maximum CAPE value of 600–800 J/kg (w ~35–40 m/s) was recorded in the vicinity of the storm. Xu et al. (2015) also reported high CAPE values during the three-year study of CGWs in China, using a network of airglow all-sky imagers. They found that during the summer months where the occurrence of the CGW events were frequent, high CAPE values obtained from the ECMWF were observed. An average CAPE value of 2,500 J/kg (w ~70 m/s) was used as the criterion for the strong instability, which may lead to thunderstorm formation and consequently overshooting of the tropopause. A relationship between GWs excited through overshooting of the tropopause by updrafts estimated from CAPE has been established through a simulation study by Vadas and Fritts (2009). They found that the amplitudes of the excited GWs were related to the vertical updraft velocities.

Besides using CAPE to study the stability of the troposphere, precipitation was also used to further demonstrate the existence of convective systems during the nights of the CGW events. A good correlation was observed between the spatial distributions of the CAPE and precipitation presented in Figure 3 and their corresponding convective systems for each event in Figure 2, except for the elliptical event (Figure 3c). For events 1 (Figure 3a) and 2 (Figure 3b), the correlation between the precipitation and convective system further affirms the presence of convective systems during the CGW events presented in this work. However, in the case of event 3, the MERRA-2 vertical wind between the altitudes of 10–20 km and 12:00–21:00 UT was eastward and southeastward. This explains the eastern and southeastern displacement of the precipitation and the deep convection with respect to the CAPE map.

The existence of the convective systems was further proven using the observed daily precipitation. These data were obtained from the Center for Weather Forecasting and Climate Studies (CPTEC) of the National Institute for Space Research (INPE). The daily precipitation data for each day of the CGW event was used. The data used here is a combination of precipitation products obtained from satellite and ground-based observation. The satellite observation was from the Tropical Rainfall Measuring Mission whereas, the ground-based observations were obtained from rain gauge datasets distributed over South America. The technique used to combine these two products is known as MERGE. Details on the precipitation datasets and the MERGE technique can be found in Rozante et al. (2010) and Rozante et al. (2020). The precipitation data for each CGW event was selected, such that if the wave was observed at the end of the day, for instance, 11 March 2008 and 25 May 2019, the data for the same day was considered. In the case of the 9 September 2016 event where the wave was observed in the early hours of the day, the precipitation of the previous day was used. This is because backward and forward ray tracing showed that the convective systems to the west of the observation site generated waves in the late hours of 8 September 2016 that were observed by the OH imager. Note that no precipitation was observed in the early hours of 9 September 2016 (i.e., 00:00–06:00 UT).

A complementary method to estimate the likely source locations of CGWs is the determination of the geometric center of the concentric wavefronts. Vadas, Yue, et al. (2009) explained through simulations the effect of the wind on the Doppler shifting of the position of the wave source relative to its propagation and distortion of the concentric structures. For the former, if the wind is weak (e.g., Nyassor et al., 2021; Vadas et al., 2012; Vadas, Yue, et al., 2009; Yue et al., 2009), that is, <30 m/s, little or no significant displacement of the ray traced source position, and the geometrically determined center is expected. Also, with weak winds, no significant distortion of the concentric wavefront will occur. In panel (a(i)) of Figure 2, the geometrically determined center, the tropopause or stopping position of the model wind ray path are close to each other, indicating weak background wind relative to the phase speed of the CGWs.

For the second event, that is, 9 September 2016, no convective system was present ±1 hr within the estimated time when the model wind ray path reached the tropopause. Rather, the nearby active convective system was observed within a distance of more than 1,000 km westward the observation site. The position of the center determined geometrically is ~300 km away from the tropopause or stopping position of the ray path (see panel (b(i)) of Figure 2), despite the wind being ≤30 m/s. If the wind is strong, that is, >30 m/s (Vadas, Yue, et al., 2009), on the other hand, distortion of the concentric structure and also, significant displacement in the location of the possible source relative to its propagation is expected. This characteristic was seen in the case of the 25 May 2019 CGW event (see panel (c(i)) of Figure 2): (a) the geometrically determined center was far from the tropopause

or stopping position of the ray path, and (b) the shape of the CGWs was distorted. Ideally, without significant concentric structure distortion observed, CGWs must appear to have ∼360° complete circular structure.

5. Discussion

This section presents detailed discussions of each of the results of the three CGW events presented in Section 4.

5.1. 11 March 2008 CGW Event

CGW events presented in this work were visible in the OH images for approximately 1 hour. The tropopause or stopping position of the model wind ray path of the 11 March 2008 CGW event was close to nearby deep convective systems. The positions of the zero wind ray path (not shown) of this event and the geometrically determined center were found to be close, that is, 6.59°S, 37.94°W for zero wind and 6.65°S, 38.18°W for the determined center. The zero wind propagation time of this wave from the tropopause to the OH emission altitude was 1 hr, 23 min. Also, a comparative method of propagation time estimation using four known parameters in the GW dispersion relation (Vadas et al., 2012) under the assumption of zero wind was employed. This propagation time (Δt) can be expressed as:

$$\Delta t = \frac{2\pi R^2 \left(1 + \Delta z^2 / R^2\right)^{3/2}}{N \Delta z \lambda_H}, \tag{4}$$

where R is the innermost radius of the concentric structures, N is the Brunt Väisälä frequency, Δz is the distance between the excitation altitudes (tropopause) to the observation altitude (OH emission layer), and λ_H is the horizontal wavelength of the wave. The result obtained from Equation 4 revealed that the propagation time for the 11 March 2008 CGW event was 1 hr, 42 min. On the other hand, using the model wind ray traced path, the tropopause position was found at 6.77°S, 38.43°W, and the propagation time was 1 hr, 42 min.

To further investigate and explain the effect of the wind on the propagation of CGW event of 11 March 2008, the vertical profiles of the zonal (light red solid line) and meridional (light blue solid line) wind in panel (a(iii)) of Figure 2 were used. Considering the background wind along the ray path of the wave, it was observed that the magnitude of the meridional wind for this event was lower than 20 m/s. The zonal wind, on the other hand, for this event varied between 45 m/s west and 34 m/s east. For the CGW event of 11 March 2008 in particular, the variations in the zonal wind was mainly westward and this has altered both the horizontal (see panel (a(i)) of Figure 2) and vertical (see panel (a(ii)) of Figure 2) propagation of the wave.

The estimated source locations of the 11 March 2008 CGW event by the ray tracing were found close to active convective systems, suggesting this CGWs was most likely generated by nearby convective systems. Prior to the observation of this event, the CAPE map (panel a(i) of Figure 3) showed high values of CAPE near the estimated source locations. Also, the spatial distribution of the precipitation (see panel a(ii) of Figure 3) during this event correlated well with the distribution of the CAPE and convective systems. Furthermore, the estimated source locations using ray tracing and the geometrically determined center all pointed to a nearby active convective source. Also, the estimated propagation times by ray tracing and Equation 4 are similar. The ray tracing and determined center identifying a similar source location indicate that this CGWs is generated by the nearby deep convection, whereas, the similar propagation times estimated using ray tracing and Equation 4 indicate that the background could not alter much the propagation of the 11 March 2008 CGW event.

5.2. 9 September 2016 CGW Event

The 9 September 2016 event had neither an active convective system present near the position where the ray path reached the tropopause nor close to the determined CGW center. Weak wind was observed during the entire wave propagation. Variations in the vertical profile (panel (b(iii)) of Figure 2) were observed with the wind being mostly westward below 52 km. The horizontal propagation in longitude and latitude (panel (b(i)) of Figure 2) and vertical propagation of this wave with time (panel (b(ii)) of Figure 2) revealed the wind could not alter much the wave trajectory. Considering the time when the ray path of 9 September 2016 reached the tropopause, the CAPE map showed no activity around the determined center and the ray path stopping position as shown in panel b(i)

of Figure 3. The spatial distribution of daily precipitation presented in panel b(ii) of Figure 3 also showed no precipitation near the center and tropopause position of the ray path.

The absence of an active convective system as shown in panel (b(i)) of Figure 2 suggests two possible generation mechanisms: (a) the wave could be generated by a far or remote convective system and propagated through a duct to the observation site, and (b) the primary waves excited by the convective system broke and generated secondary GWs, which then propagated to the field of view of the all-sky imager. Between 22:00 UT on 8 September 2016 and 04:00 UT on 9 September 2016, convective systems with cloud top brightness temperatures ranging from −60°C to −70°C were observed. This system was more than 1,000 km (centered around 51°W, 9°S and 48°W, 2°S) away from the observation site. The 30 min resolution infrared CTBT images within the above-stated time range showed no significant spatial displacement.

5.2.1. Propagation of the Observed CGWs in a Duct Condition

To explore the former possibility, the condition of the background atmosphere was investigated. During this CGW event, eight sounding positions of the TIMED/SABER satellite were obtained. Five soundings among the eight were selected to be used in the study of the background atmosphere. Three of the soundings close to the observation site within the time interval of 02:52 UT to 02:56 UT on 9 September 2016, and two close to the convective system within the interval of 04:31 UT to 04:32 UT were chosen. In panel (a) of Figure 4, the kinetic temperature profiles of the five soundings are presented, whereas in panel (b) is the composite plot of the five profiles in panel (a). The average of the individual profiles (in light red) in panel (b) is the black solid profile. In panel (c), the composite CTBT map of the convective system and the corresponding sounding positions of each profile in panel (a) is shown. The closest sounding positions to either the convective system or to the observation site are depicted by the squares with their corresponding colors of the sounding times defined in the legends for the five profiles. The positions and times of each sounding are defined in the legends in panel (c).

Note that the three gray squares in panel (c) of Figure 4 were not considered. This is because two of the gray squares (between latitudes −2° and 1°) were far from the convective system and the observation site. The remaining gray square, on the other hand, did not meet the criteria used in the classification of an inversion layer. The procedure of the mesospheric inversion layer (MIL) classification follow the work of Leblanc and Hauchecorne (1997) and Fechine et al. (2009). The profile with MIL to be selected must satisfy the following criteria: the bottom of an inversion should be 5 km above the stratopause and the top should be below 90 km; the MIL amplitude, that is, the difference between the temperature at the top and the bottom level should be greater than 10 K and less than 100 K; the MIL thickness, that is, the difference between the altitude at the top and the bottom level should be greater than 4 km. The gray shaded regions within the altitude range of ∼74–82 km in panel (a(i–v)) of Figure 4 emphasize the MIL in the temperature profiles.

Figure 5 shows the profiles of the average temperature (black profile in Figure 4b), potential temperature (θ), Brunt Väisälä frequency squared N^2, neutral wind, the vertical wavenumber squared m^2, and the OH volume emission rate (VER). These profiles were calculated along the ray path of the GWs as shown in Figure 2b. Figure 5a shows the kinematic temperature (solid line) and potential temperature profiles (dashed line). The θ can be obtained using

$$\theta = T\left(\frac{p_o}{p}\right)^{R/c_p}, \tag{5}$$

where T is the temperature in K, p_o is the standard pressure, p is the atmospheric pressure, R is the gas constant and c_p is the specific heat capacity at constant pressure. The Brunt Väisälä frequency (Figure 5b) is estimated using:

$$N = \sqrt{\left(\frac{g}{\theta}\right)\frac{d\theta}{dz}}, \tag{6}$$

where g is the gravitational acceleration. The neutral wind profile is derived from the model winds (concatenated MERRA-2 and HWM14) since no neutral wind u observations were available during that night.

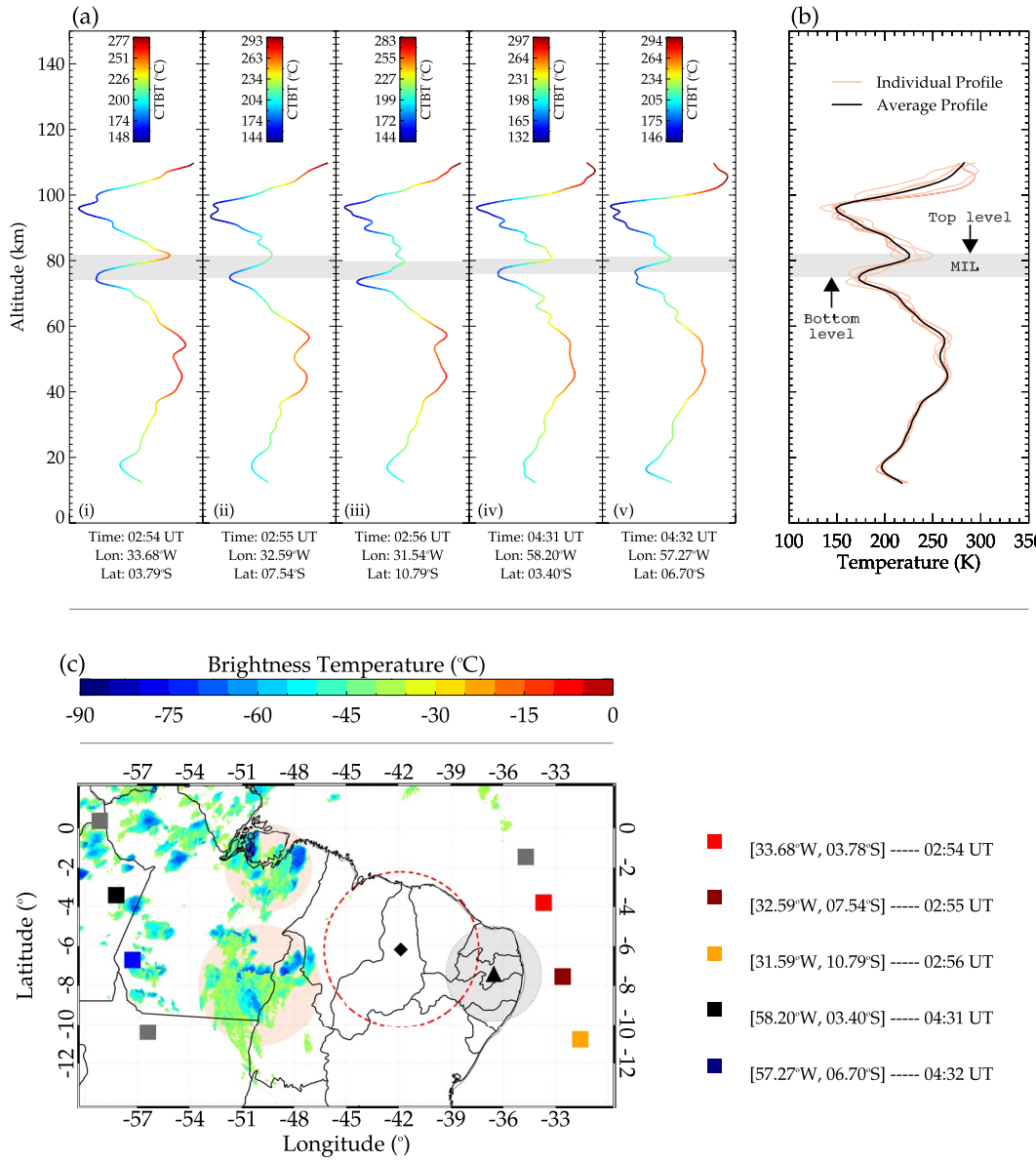

Figure 4. Kinetic temperature profile (a) of five SABER soundings (positions of each profile is shown by the squares in panel (c) with their times defined in the legends). The average profile (black) of the individual profiles (light red) is shown in panel (b). In panel (c) the active convective system during this event is shown. The light red shaded regions emphasizes the principal regions of the convective system. The gray circular region depicts the field of view of the all-sky imager. The triangle, diamond, and dashed red circle are the same as those defined in Figures 2 and 3. The color bar is the temperature scale of the cloud top brightness temperature (CTBT) image overplotted in panel (c).

Studying GWs propagation in the atmosphere requires m^2, which is dependent on the wind shear and temperature gradient (Yiğit et al., 2009). The estimated m^2 was adapted from the dispersion relation of GWs used in the ray tracing according to Vadas (2007):

$$m^2 = \frac{k_H^2 N^2}{\omega_{Ir}^2 (1 + \delta_+ + \delta^2/\mathrm{Pr})} \left[1 + \frac{\nu^2}{4\omega_{Ir}^2} \left(\vec{k}^2 - \frac{1}{4H^2} \right)^2 \cdot \frac{\left(1 - \mathrm{Pr}^{-1}\right)^2}{(1 + \delta_+/2)^2} \right]^{-1} - k_H^2 - \frac{1}{4H^2}, \quad (7)$$

where $\delta_+ = \delta(1 + \mathrm{Pr}^{-1})$, $\nu_+ = \nu(1 + \mathrm{Pr}^{-1})$, $\nu = \mu/\rho$, and $\delta = \nu m/H\omega_{Ir}$, H is the density scale height, ρ is the density, Pr is the Prandtl number, ω_{Ir} is the intrinsic frequency, $\vec{k}^2 = k_H^2 + m^2$ is the wavenumber with $k_H^2 = k^2 + l^2$ being

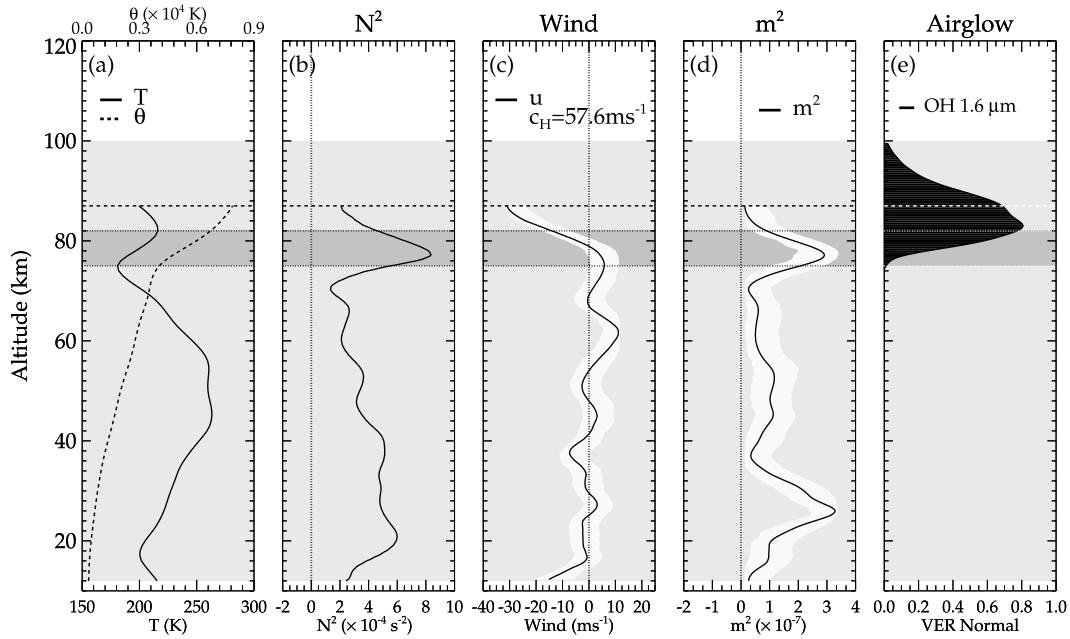

Figure 5. Background analysis during the 9 September 2016 concentric gravity wave event over São João do Cariri. Panel (a) is the average kinematic temperature profile (black solid line in Figure 4(b)) obtained by the TIMED/SABER satellite and the potential temperature θ (dotted line). In panel (b), the squared Brunt-Väisälä frequency N^2 is shown and (c) the wind speed (solid line) is presented. Panel (d) is the vertical wavenumber squared (m^2) and (e) the normalized volume emission rate (VER) profile of the OH at 1.6 µm are shown.

the horizontal wavenumber and m^2 being the vertical wavenumber. More details on Equation 7 can be found in Vadas and Fritts (2006) and Vadas (2007).

Panel (d) of Figure 5 shows the m^2 profile depicted by the solid line. The white shaded region around the profiles of the wind (panel (c)) and the m^2 (panel (d)) indicate the error range. The maximum error for the wind is $\sim\pm5$ m/s and $\sim\pm1.2\times10^{-7}$ for m^2. The error in u and m^2 was estimated by calculating the propagation error. This procedure follows the propagation error analysis of Bevington and Robinson (2003). To estimate this error, the standard deviation of each variable is computed and multiplied by the derivative of the variable with respect to altitude. The sum of the product of the variables and their derivatives at each altitude is the propagation error. In panel (e) the normalized volume emission rate (VER) profile of the OH at 1.6 µm (black shaded region) measured by the TIMED/SABER satellite is shown. The gray-shaded region emphasizes the inversion layer. The horizontal dotted lines above and below the gray shaded region in all sub-figures indicate the top and bottom of the MIL, whereas the light-gray shaded regions emphasize the altitude range from 12 to 100 km. The horizontal dashed line indicates the 87 km (OH emission) altitude.

During this wave event, the VER of the 1.6 µm OH profile extended from 70 to 100 km with a peak at ~83 km. Since we are interested in studying the propagation of the waves between the excitation and observation altitudes, only profiles below 87 km were considered. The MIL in the temperature profile was between ~74–82 km. However, no effect of this inversion layer could be seen in the m^2 profile. The m^2 was positive ($m^2 > 0$) throughout the entire profile suggesting the CGW was propagating (Gossard & Hooke, 1975).

Ducting and propagation of GWs are mainly controlled by the background winds, however, the CGW being ray traced here was not affected by a duct. Note that the MERRA-2 winds below 70 km and the HWM14 climatology winds above 70 km (monthly averages) may differ from the actual winds. Previous studies (e.g., Bageston et al., 2011; Carvalho et al., 2017; Fechine et al., 2009; Simkhada et al., 2009; Snively et al., 2007) demonstrated the importance of winds in the formation of Doppler duct at the mesospheric heights to allow long-distance horizontal propagation of GWs at this altitude. The effects of thermal ducts, on the other hand, have been highlighted by Bageston et al. (2011). Despite the inability of the wave to be ducted in the ray tracing model, the possibility of ducting cannot be excluded especially the Doppler duct (Kogure et al., 2020).

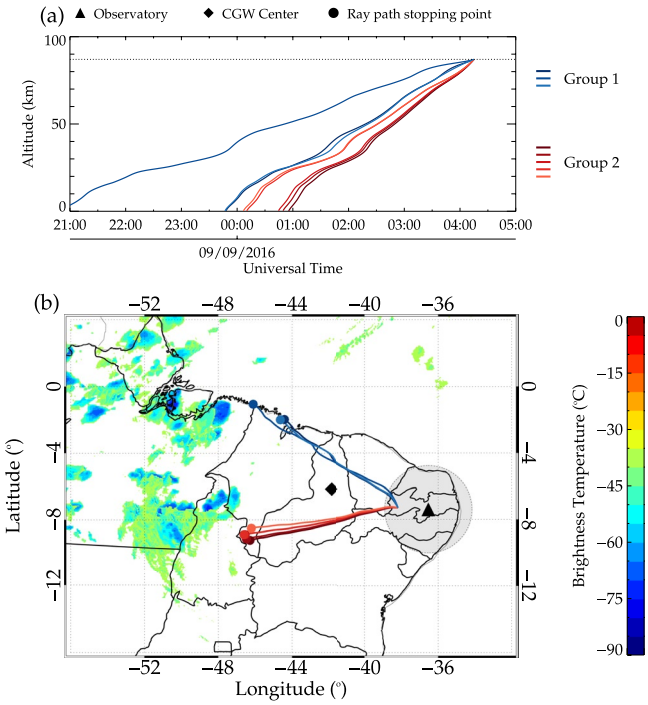

Figure 6. Two groups of medium-scale gravity waves (MSGWs). In panel (a), the time-altitude variations of the model wind ray paths are shown, whereas panel (b) shows the longitude and latitude variation of the model wind ray paths. The gray circular region depicts the field of view of the all-sky imager. The triangle and diamond are the same as those defined in Figures 2 and 3. The filled circles of each respective color show the ray path stopping position. The color bar is the temperature scale of the cloud top brightness temperature image overplotted in panel (b).

5.2.2. Observed Gravity Waves Generated by Convective System

Besides the observed CGWs in the OH emission layer, medium-scale gravity waves (MSGWs) have been observed as well. These observed MSGWs were visible in the OH images around 04:00 UT before the CGWs first appeared at 04:49 UT. The time difference (TD) OH image and keogram with MSGWs signatures can be found in Figures S4 and S5 of the Supporting Information S1. The purpose of introducing the MSGWs is to show that other spectrum of GWs generated by the far away convective system propagated to the field of view of the imager. Also, the MSGWs will be used to demonstrate that this CGW could not propagate directly from the location of the associated convective system to the field of view of the all-sky imager. Figure 6 shows the results of two groups of backward ray traced MSGWs.

In Figure 6a, the time-altitude variations of the model wind ray paths are shown, whereas panel (b) shows the longitude and latitude variations of the model wind ray paths. The color bar shows the scale of the cloud top brightness temperature (CTBT) over plotted together with the ray paths in panel (b). The GOES infrared (IR) CTBT in Figure 6 is a composite image of CTBT at 21:00 UT, 22:00 UT, and 23:00 UT on 8 September 2016 and 00:00 UT on 9 September 2016. These four (4) CTBT were considered because: (a) there was no significant change in the position of the convective system within this time frame and (b) the times when the ray paths of the waves reached the tropopause. The triangle, diamond, and filled circle show the location of the observation site, the center of the CGWs, and the location where the ray tracing for each MSGWs stopped, respectively. The gray-filled circular region with a dotted circle shows the field of view of the all-sky imager. The time the ray tracing began for all the waves in Figure 6 is taken to be 04:15 UT since these waves were observed between 03:00 and 04:30 UT. The colors of each ray path show the groups of MSGWs backward ray traced. The grouping is based on their propagation directions and horizontal wavelengths. In Figure 7, the parameters of the MSGWs are summarized. In panels (a), (b), (c), and (d), the horizontal wavelength (λ_H), period (τ), phase speed (c_H), and propagation direction (ϕ) measured clockwise from the north, respectively, are shown. Each color in the group corresponds to their respective ray paths colors in Figure 6.

As shown in Figure 7, the propagation directions of the waves are in agreement with the locations of the convective systems relative to the location of the observation site. Dare-Idowu et al. (2020) investigated the sources of GWs with medium-scale parameters and planar wavefronts at the same observation site. Using reverse ray tracing, they identified convection systems northwest of the observation site as their possible source. These ray tracing results clearly show that the convective systems most likely generated the waves in groups 1 and 2. Here, the backward ray tracing paths show that the MSGWs were most likely excited by these convective

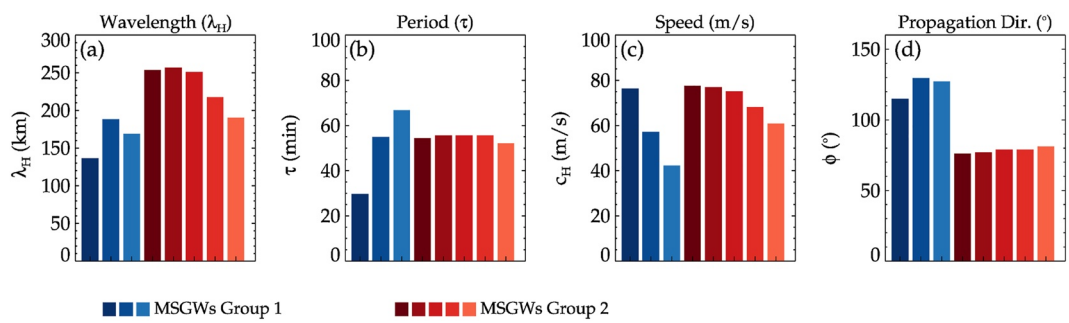

Figure 7. Characteristics of medium-scale gravity waves observed during the 9 September 2016 concentric gravity waves event.

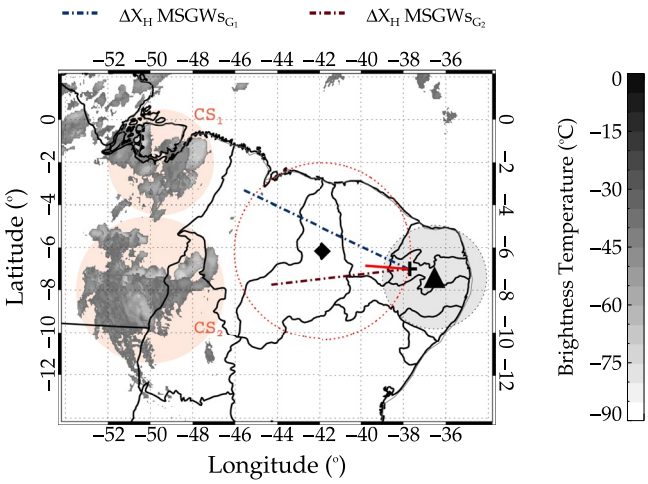

Figure 8. The geometry of horizontal distance traveled by medium-scale gravity waves (MSGWs) Group 1 ($MSGWs_{G1}$) and medium-scale gravity waves Group 2 ($MSGWs_{G2}$) with respect to the convective systems, CS_1 and CS_2. The light red circular shaded region emphasizes the regions of convective systems 1 and 2. The cloud top brightness temperature and its color scale are similar to that of Figure 6 except for the representation in greyscale. The gray shaded circular region represents the field of view of the imager and the triangle shows the location of the all-sky imager. The diamond indicates the center of the first concentric wavefront in the OH image which is indicated by the red dotted circle. The plus symbol shows where the ray tracing began. The dark blue dashed-dotted line shows the maximum horizontal distance travel by the waves in $MSGWs_{G1}$, whereas the dark red dashed-dotted line shows the maximum horizontal distance travel by the waves in $MSGWs_{G2}$. The red solid line shows the maximum horizontal distance traveled by the concentric gravity wave.

systems and observed by the São João do Cariri imager. Since model winds were used in the ray tracing, this could only give us an idea about the state of the atmosphere. We now estimate the horizontal propagation distance of these waves using the periods of the wave and that of Brunt Väisälä, adapting the approach of Vadas and Crowley (2010).

We chose the maximum wave period (τ) of ~66 min from MSGWs group 1 and ~55 min from MSGWs group 2. The Brunt Väisälä period (τ_B) was taken to be 5 min. The tropopause altitude determined from the radiosonde measurement was 17 km. Therefore, the vertical distance (Δz) between the top of the cloud and the observation altitude at 87 km is 70 km. The horizontal propagating distance ΔX_H is

$$\Delta X_H = \Delta z \frac{\tau}{\tau_B}. \quad (8)$$

From Equation 8, the horizontal distance traveled by a ~66 min wave of the MSGWs group 1 was ~933 km whereas that of MSGWs group 2 was ~778 km. It can be observed that the estimated horizontal distance traveled by both MSGWs in Groups 1 and 2 agree with the distance between the positions of the convective systems and the observation sites. To confirm and affirm the horizontal distance traveled by the MSGWs, we also forward ray traced the same groups of waves presented in Figure 6. These forward ray traced waves also propagated close to the field of view of the imager.

5.2.3. Source Location of Observed 9 September 2016 CGW Event

As shown in panel (b(i)) of Figure 2, the ray tracing stopping or tropopause position was not close to any nearby active convective system. Also, it was observed that the background wind could not change the wavevector that will cause the wavefronts to have partial concentric structure. As a result, the only possible source could be body forces created through momentum and energy deposition by breaking primary waves. However, our ray tracing did not stop anywhere but in the troposphere. It was expected that the ray path should have stopped in the upper stratosphere or lower mesosphere or better still ducted. However, this must not be the case since the parameters of secondary gravity waves do not always have to meet the stopping conditions around their sources. Ducting and the ray tracing stopping conditions of GWs mainly depend on the background wind and temperature. During this CGW event, no observed wind was available, and therefore, we cannot estimate the actual background wind, which may affect the interpretation of our result.

On the other hand, the locations of the nearby convective systems considered as the possible source of the primary MSGWs are found to be ~550 km away from the estimated center of the CGW. Considering the wave was excited at 17 km and propagated to the OH emission altitude (~87 km), we have Δz ~70 km. Taking τ_B ~5 min, τ ~12 min, and using Equation 8, ΔX_H ~172.2 km. The relationship between the MSGWs, CGW, and the convective system are graphically presented in Figure 8.

In Figure 8, the estimated horizontal propagation distances traveled by the MSGWs and the CGW with respect to the convective system is shown. The dark blue and red dashed-dotted lines represent the horizontal distance traveled by the MSGWs in Groups 1 and 2, respectively. The red solid line represents the horizontal distance traveled by the CGW. The light red circular shaded region emphasizes the regions of convective systems 1 and 2. The CTBT and its color scale are similar to that of Figure 6 except for the representation in greyscale. From Figure 8, it is clear that the possible horizontal distance, the CGW is expected to propagate cannot exceed longitude −46° if we consider the excitation point to be −48°. This distance is not even up to half the distance between the center of the CGW and the excitation point (which is taken to be −48°). This, therefore, implies the CGW event on 9 September 2016 could only propagate this distance from the convective system in either direction, that is, toward CS_1 or CS_2. This analogy further shows that the only way the CGW with such characteristics can propagate to the imager's field of view is through ducting or it originated from other possible source.

This other possible source of the 9 September 2016 CGW event can be convective instability due to GWs breaking. Various studies (e.g., Heale et al., 2020; Kogure et al., 2020; Vadas & Azeem, 2020; Vadas & Becker, 2019) mentioned that convective instabilities may occur in the regions of wave breaking. The exponential growth of wave amplitudes with height as a consequence of the decreasing background density is damped by convective instability when the amplitude $|u'_H|$ exceeds the instability threshold at the breaking altitude where

$$\frac{|u'_H|}{|c_H - U_H|} \simeq 0.7 - 1.0 \tag{9}$$

(Fritts & Alexander, 2003; Vadas & Becker, 2019; Yiğit et al., 2008). Here $u'_H = \sqrt{(u')^2 + (v')^2}$ is the horizontal wind perturbation of the GW, u' and v' are the zonal and meridional wind perturbations, c_H is the ground-based horizontal phase speed and U_H is the background horizontal wind along the direction of GWs propagation.

Vadas and Becker (2019) and Kogure et al. (2020) used this condition as a proxy for gravity waves breaking or saturation (corresponding to convective instability) prior to their secondary GW events. This condition was not satisfied by the primary MSGWs presented in this current work. Even though the Atmospheric Infrared Sounder on NASA's Aqua satellite made observations during this wave event, no GWs perturbations were observed in the stratosphere near the convective system that can be used to study wave originating from the convective system. Hence, to investigate in detail GWs activity in the stratosphere and lower mesosphere, a simulation study needs to be conducted. For this present work, simulation is out of the scope, thus a complementary paper on simulation study specifically for 9 September 2016 will follow.

In summary, two possible sources of the 9 September 2016 CGW have been explored. First, the convective system was investigated and found not to be the most likely source of this CGW. The background studies conducted showed that no duct, neither thermal nor doppler was present to enhance longer horizontal propagation if the CGW was excited by the convective systems. However, these convective systems were far away from the center of the CGW. Observed data such as precipitation and model CAPE data showed high precipitation and CAPE activity around the location of the convective systems. This further proves that the deep convection is most likely not the source of this CGW thus, it might originate from other source mechanisms. Another source of CGW generation can be instabilities created by body forces when GWs break (Kogure et al., 2020; Vadas & Becker, 2019).

The convective instability was computed along the ray paths of the MSGWs (considered as primary GWs) but found none to attain this condition along it path. It is important to mention that the ray tracing model used in this work cannot determine nonlinear interactions (Yiğit & Medvedev, 2015). Due to lack of GWs observation in the stratosphere and lower mesosphere, detail analysis could not be performed. This possibility, nonetheless, can only be investigated through numerical simulation. A detailed numerical study is beyond the scope of this work, but can be suitable for future work.

5.3. 25 May 2019 CGW Event

In the case of the 25 May 2019 CGW event, there was a deviation in the model wind ray tracing estimated stopping or tropopause position and the center of the elliptical wavefront. The study of the tropospheric stability during the time of wave excitation using CAPE map presented in panel c(i) of Figure 3 shows strong CAPE activity. Besides CAPE activities being high during this excitation time, precipitation (see panel c(ii) of Figure 3) further confirms the existence of deep convective systems as revealed by the GOES-16 IR image overplotted in panel c(i) of Figure 2. As stated earlier, this event was semi-elliptical in shape, which is the first evidence of relatively strong and varying wind. The final position of the model wind ray path was 5.57°S, 37.74°W, while the estimated center of the ellipse was at 4.60°S, 37.57°W. This shows the estimated center was ∼107 km away from the tropopause or stopping position of the model wind ray traced path.

The estimated propagation time using the major axis of the ellipse was ∼50 min, whereas that of the model wind ray path was ∼35 min. However, the ray path of the zero wind stopped at ∼70 km, due to the violation of the condition, $m^2 \gg 1/4H^2$ or $\lambda_z < 4\pi H$ in the anelastic dispersion relation (Vadas & Fritts, 2005, 2006). Besides the difference observed between the position of the determined center of the ellipse and the ray path tropopause position, there is a difference in the propagation times as well. Based on these characteristics, the wind is expected to be strong and varying, as shown in the simulation result of Vadas, Yue, et al. (2009) and observed by Xu et al. (2015). Besides the semi-elliptical wavefronts, differences in the positions of the determined center,

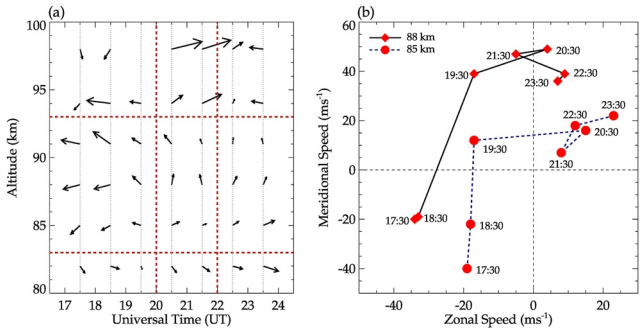

Figure 9. Mesospheric wind characteristics during the 25 May 2019 concentric gravity wave event. (a) The vector plot of the horizontal wind component. (b) Hodograph of the wind at altitude 88 km (solid black lines with red diamonds) and 85 km (dark blue dashed lines with red dots).

convective system, and tropopause of the model wind ray path were also observed. These differences are explained using observed wind from meteor radar. In Figure 9, the vector plot (panel (a)) and the hodograph (panel (b)) of the meteor radar wind are shown.

The meteor radar operates at the same location as the airglow imager. The radar works at a frequency of 35.24 MHz, with a transmitter power of 12 kW. It measures wind velocity from 82 to 100 km at a height interval of 3 km and a temporal resolution of 1 hr. The vector plot in panel (a) of Figure 9 ranges from 82 to 98 km and from 17:30 to 23:30 UT. The two red dashed vertical lines were used to demarcate the time range of 20:00–22:00 UT, whereas the two horizontal lines are used to demarcate the height range of 83–93 km. As depicted, the wind vector was mostly westward at heights 85–95 km between 17:30 UT and 18:30 UT. The direction began rotating toward the north around 19:30 UT and was mainly northwestern at 85 and 88 km of altitude. The rotation of the wind toward the northwest within the mesosphere may be responsible for the northwestward shifting of the center of the 25 May 2019 CGW event relative to the convective system (the possible source).

Also, the hodograph at 85 and 88 km showed a northeast dominant wind and a change in direction between 19:30 and 21:30 UT. This dominant wind and its change in direction could be responsible for the compression of the sides of the concentric structure, thereby, forming the elliptical wave shape. It is also important to mention that the two factors that determine the distortion effect of the wind on wavefront, that is, variations in group velocity and wavevector along the wave path were observed as well. The characteristics of the wind at heights 85 and 88 km used to explain why the concentric structure looks elliptical, is similar to the approach described by Xu et al. (2015).

Besides the wind in the MLT region, the wind from the tropopause (i.e., 16 km) to this region is equally an important determining factor of the distortion effect of the wind on concentric rings of GWs (Vadas, Yue, et al., 2009). As mentioned by Vadas, Yue, et al. (2009), the waves spend a longer propagation time from the tropopause to 80 km than 80–87 km. Thus, distortion of wavefronts of the CGWs occurs when the wind is nonzero in the atmosphere causing them to appear as "squashed" rings and "partial" arcs.

Xu et al. (2015) mentioned that background wind distorts airglow CGWs (Vadas, Yue, et al., 2009). In their study, they observed GWs with an elliptical wavefront on the night of August 13–14, 2013, near the Shuozhou (39.8°N, 112.1°E) station. Using a meteor radar wind with a 2 km height interval and 1 hr temporal resolution, they showed the wind characteristics at 87 km between 20:00 LT on 13 August 2013, to 04:00 LT on 14 August 2013. Using a hodograph of the wind at 87 km altitude (their figure 11), the wind direction was almost southeastward between the hours of 20:00-03:00 LT. The wind was found to be decreasing from 58 m/s at 20:00 LT to 10 m/s at 04:00 LT. The background wind characteristics during this event were consistent with that of the background wind during the observed elliptical GW event of Xu et al. (2015).

The eastward and southeastward propagation of the CGW events on 11 March 2008 and 25 May 2019, suggest these waves were excited in the western and northwestern part of the observation site, respectively. Indeed, intense and active convective systems were found in these regions where the ray tracing has indicated as the possible source locations. The eastward and southeastward propagation of the waves cannot only be explained by the presence of a convective system during the night the waves were observed but also the season of the year. The season within which these waves were observed corresponds to the season where the Intertropical Convergence Zone (ITCZ) is near the equator. Dare-Idowu et al. (2020) attributed the waves presented in their work propagating in a similar direction to the presence of convection during the season of the ITCZ. Previous works (e.g., Dare-Idowu et al., 2020; Essien et al., 2018) and the current identified GWs sources within the months of autumn are in agreement with the times of the action of ITCZ in Brazil, as shown by Utida et al. (2019). The final position of the ray path of the 11 March 2008 and 25 May 2019 CGW events agreed with the identified convective system positions.

The 25 May 2019 CGW event, on the other hand, presented quite different propagation characteristics relative to the geometrically determined center. Even though the model wind was weak and could not fully explain

the observation, it gave an idea of the state of the wind during this wave event and also the propagation of the observed CGW. Since primary CGWs indicate a point-like overshooting of the tropopause (Nyassor et al., 2021; Xu et al., 2015; Yue et al., 2009), and elliptical wavefront of CGWs indicate strong and varying winds (Vadas, Yue, et al., 2009; Xu et al., 2015), this CGW is most likely generated by the nearby convective system, suggesting it is a primary gravity wave. The elliptical shape of 25 May 2019 CGW was explained using the observed wind from meteor radar.

6. Summary and Conclusion

This work has presented three selected CGW events observed in the OH airglow emission layer over São João do Cariri in the equatorial region of Brazil. The events presented different propagation characteristics and wavefront configurations. Two of these events have arc-like wavefronts, whereas one had semi-elliptical wavefronts. A backward ray tracing model was used to study the propagation characteristics from the OH emission altitude to the likely source position. In all three events, the model wind showed weak winds from the ray traced regions of wave generation to the location of their observation.

The stopping or tropopause positions of the ray tracing of the CGW event on 11 March 2008 suggests this wave was excited by convective systems through overshooting. The respective times when the ray path reached the tropopause agreed with the times when GOES IR CTBT images had the coldest brightness temperature suggesting convective overshooting. A comparison between the estimated source positions from the ray tracing and the geometrically determined centers using the first visible concentric crest on the image was also made. Good agreements were observed between the position of the center of the wave and the source position determined by the ray tracing for the 11 March 2008 CGW event.

The CGW event on 9 September 2016 presented different propagation characteristics relative to its source location. No active convective system was seen at the time the ray traced path reached the tropopause. The nearby active convective system present was more than 1,000 km away from the observation site. Background investigation on the vertical wave propagation condition showed no ducts in the lower atmosphere or the mesopause region even though there was a temperature inversion layer between 74 and 82 km as observed by SABER instrument. Therefore, ducting of the CGW was considered less probable for a longer horizontal wave propagation since there was no observed wind during the night of the event.

From backward ray tracing, some observed primary MSGWs were found to be excited by the remote convective system. Also, a numerical estimate of the horizontal wave propagation showed that the MSGWs were most likely excited by the convective systems. Considering now the horizontal distance the observed CGW was expected to travel, we found that a wave with such characteristics could not have been generated by the convective systems. This leaves us with not only the possibility of body force mechanism but also other possible mechanisms of GWs generation which will be explored in future work.

In the case of the CGW event on 25 May 2019, the stopping or tropopause position of the ray path coincides with the location of nearby active convective systems. However, the determined center and the source positions were distant from each other. This difference was explained using the northwestward horizontal wind obtained from the meteor radar before and during this event. Also, a hodograph of the meteor radar wind at altitudes 85 and 88 km was used to explain the observed semi-elliptical wavefront of the 25 May 2019 CGW event.

Finally, among the three CGW events presented in this work, the events on 11 March 2008 and 25 May 2019 most likely originated from tropospheric deep convection. The 9 September 2016 CGW event, on the other hand, showed that this event was not directly linked to the convective systems that excited other observed primary MSGWs. Also, background studies showed that this wave might not be ducted. Therefore, simulation and further studies are needed to complement 9 September 2016 CGW event to investigate the source of this wave and also its propagation.

Data Availability Statement

Airglow images from São João do Cariri can be accessed online in the portal of the "Estudo e Monitoramento Brasileiro do Clima Espacial" (EMBRACE/INPE) at http://www2.inpe.br/climaespacial/portal/en/. The cloud top brightness temperature maps and precipitation data were provided by the Center for Weather Forecasting and Climate Studies (CPTEC/INPE) at http://satelite.cptec.inpe.br/acervo/goes16.formulario.logic. Radiosonde data were obtained from the University of Wyoming through the link http://weather.uwyo.edu/upperair/sounding.html. CAPE ERA5 re-analysis data were provided by the European Centre for Medium-Range Weather Forecasts (ECMWF) at https://cds.climate.copernicus.eu/%23%21/home (Hersbach et al., 2018). The MERRA-2 wind and temperature data set is accessible at https://daac.gsfc.nasa.gov/datasets/M2I3NVASM5.12.4/summary (Modeling & (GMAO), 2015).

Acknowledgments
A special thanks goes to Sharon L. Vadas for her inputs and suggestions regarding the CGWs. This work has been supported by the Coordenação de Aperfeiçoamento de Pessoal de Nível Superior (CAPES) and the Conselho Nacional de Desenvolvimento Científico e Tecnológico (CNPq). Thanks to the Brazilian Ministry of Science, Technology and Innovations (MCTI) and the Brazilian Space Agency (AEB) who supported the present work under the grant number 20VB.0009. P. K. Nyassor, C. M. Wrasse, I. Paulino, H. Takahashi, and D. Barros thank CNPq for the financial support under the contract numbers 317957/2021-0, 300322/2022-4, 314972/2020-0, 306063/2020-4, 310927/2020-0 and 300974/2020-5. I. Paulino thanks to Fundação de Amparo à Pesquisa do Estado do Paraíba (FAPESQ PB) for the PRONEX grant 002/2019 and 09/2021 Universal grant. E. Yiğit was partially supported by NASA (Grant Number 80NSSC22K0016). C.A.O.B. Figueiredo thanks the Fundação de Amparo à Pesquisa do Estado de São Paulo (FAPESP) for the support under the process number 2018/09066-8 and 2019/22548-4. The cloud top brightness temperature maps and the precipitation data were provided by the Center for Weather Forecasting and Climate Studies (CPTEC/INPE). The radiosonde data were provided by the University of Wyoming. The authors would like to thank the editor and reviewers for their helpful comments, suggestions, and corrections which improved and completely changed the manuscript.

References

Akiya, Y., Saito, A., Sakanoi, T., Hozumi, Y., Yamazaki, A., Otsuka, Y., et al. (2014). First spaceborne observation of the entire concentric airglow structure caused by tropospheric disturbance. *Geophysical Research Letters*, *41*(19), 6943–6948. https://doi.org/10.1002/2014GL061403

Alexander, M. J., Holton, J. R., & Durran, D. R. (1995). The gravity wave response above deep convection in a squall line simulation. *Journal of the Atmospheric Sciences*, *52*(12), 2212–2226. https://doi.org/10.1175/1520-0469(1995)052⟨2212:TGWRAD⟩2.0.CO;2

Azeem, I., Yue, J., Hoffmann, L., Miller, S. D., Straka, W. C., & Crowley, G. (2015). Multisensor profiling of a concentric gravity wave event propagating from the troposphere to the ionosphere. *Geophysical Research Letters*, *42*(19), 7874–7880. https://doi.org/10.1002/2015GL065903

Bageston, J., Wrasse, C. M., Batista, P., Hibbins, R., Fritts, D., Gobbi, D., & Andrioli, V. (2011). Observation of a mesospheric front in a thermal-Doppler duct over king George Island, Antarctica. https://doi.org/10.5194/acp-11-12137-2011

Bageston, J., Wrasse, C. M., Gobbi, D., Takahashi, H., & Souza, P. (2009). Observation of mesospheric gravity waves at Comandante Ferraz Antarctica station (62 s). *Annales Geophysicae*, *27*(6), 2593–2598. https://doi.org/10.5194/angeo-27-2593-2009

Bevington, P. R., & Robinson, D. K. (2003). *Data reduction and error analysis for the physical sciences* (3rd ed.). McGraw-Hill. Retrieved from https://cds.cern.ch/record/1305448

Carvalho, A., Paulino, I., Medeiros, A. F., Lima, L. M., Buriti, R. A., Paulino, A. R., et al. (2017). Case study of convective instability observed in airglow images over the Northeast of Brazil. *Journal of Atmospheric and Solar-Terrestrial Physics*, *154*, 33–42. https://doi.org/10.1016/j.jastp.2016.12.003

Dare-Idowu, O., Paulino, I., Figueiredo, C. A., Medeiros, A. F., Buriti, R. A., Paulino, A. R., & Wrasse, C. M. (2020). Investigation of sources of gravity waves observed in the Brazilian equatorial region on 8 April 2005. *Annales Geophysicae*, *38*(2), 507–516. https://doi.org/10.5194/angeo-38-507-2020

Drob, D. P., Emmert, J. T., Meriwether, J. W., Makela, J. J., Doornbos, E., Conde, M., et al. (2015). An update to the Horizontal Wind Model (HWM): The quiet time thermosphere. *Earth and Space Science*, *2*(7), 301–319. https://doi.org/10.1002/2014EA000089

Eckermann, S. D. (1992). Ray-tracing simulation of the global propagation of inertia gravity waves through the zonally averaged middle atmosphere. *Journal of Geophysical Research*, *97*(D14), 15849–15866. https://doi.org/10.1029/92JD01410

Essien, P., Paulino, I., Wrasse, C. M., Campos, J. A. V., Paulino, A. R., Medeiros, A. F., et al. (2018). Seasonal characteristics of small-and medium-scale gravity waves in the mesosphere and lower thermosphere over the Brazilian equatorial region. *Annales Geophysicae*, *36*(3), 899–914. https://doi.org/10.5194/angeo-36-899-2018

Fechine, J., Wrasse, C. M., Takahashi, H., Medeiros, A. F., Batista, P., Clemesha, B., et al. (2009). First observation of an undular mesospheric bore in a Doppler duct. *Annales Geophysicae*, *27*(4), 1399–1406. https://doi.org/10.5194/angeo-27-1399-2009

Fritts, D. C., & Alexander, M. J. (2003). Gravity wave dynamics and effects in the middle atmosphere. *Reviews of Geophysics*, *41*(1). https://doi.org/10.1029/2001RG000106

Fritts, D. C., Vadas, S. L., Wan, K., & Werne, J. A. (2006). Mean and variable forcing of the middle atmosphere by gravity waves. *Journal of Atmospheric and Solar-Terrestrial Physics*, *68*(3–5), 247–265. https://doi.org/10.1016/j.jastp.2005.04.010

Garcia, F., Taylor, M. J., & Kelley, M. (1997). Two-dimensional spectral analysis of mesospheric airglow image data. *Applied Optics*, *36*(29), 7374–7385. https://doi.org/10.1364/AO.36.007374

Gelaro, R., McCarty, W., Suárez, M. J., Todling, R., Molod, A., Takacs, L., et al. (2017). The modern-era retrospective analysis for research and applications, version 2 (MERRA-2). *Journal of Climate*, *30*(14), 5419–5454. https://doi.org/10.1175/JCLI-D-16-0758.1

Giongo, G. A., Bageston, J. V., Figueiredo, C. A., Wrasse, C. M., Kam, H., Kim, Y. H., & Schuch, N. J. (2020). Gravity wave investigations over Comandante Ferraz Antarctic station in 2017: General characteristics, wind filtering and case study. *Atmosphere*, *11*(8), 880. https://doi.org/10.3390/atmos11080880

Gossard, E. E., & Hooke, W. H. (1975). Waves in the atmosphere: Atmospheric infrasound and gravity waves-their generation and propagation. *Atmospheric Science*, *2*.

Heale, C. J., Bossert, K., Vadas, S. L., Hoffmann, L., Dörnbrack, A., Stober, G., et al. (2020). Secondary gravity waves generated by breaking mountain waves over Europe. *Journal of Geophysical Research: Atmospheres*, *125*(5), e2019JD031662. https://doi.org/10.1029/2019JD031662

Heale, C. J., Snively, J., Bhatt, A., Hoffmann, L., Stephan, C. C., & Kendall, E. (2019). Multilayer observations and modeling of thunderstorm-generated gravity waves over the midwestern United States. *Geophysical Research Letters*, *46*(23), 14164–14174. https://doi.org/10.1029/2019GL085934

Hersbach, H., Bell, B., Berrisford, P., Biavati, G., Horányi, A., Muñoz Sabater, J., et al. (2018). Era5 hourly data on single levels from 1979 to present. ECMWF, [dataset]. https://doi.org/10.24381/cds.adbb2d47

Holton, J. R. (1992). An introduction to dynamic meteorology. In *International geophysical series* (3d ed.), (Vol. 48). Academic Press.

Kogure, M., Yue, J., Nakamura, T., Hoffmann, L., Vadas, S. L., Tomikawa, Y., et al. (2020). First direct observational evidence for secondary gravity waves generated by mountain waves over the Andes. *Geophysical Research Letters*, *47*(17), e2020GL088845. https://doi.org/10.1029/2020GL088845

Lane, T. P., Reeder, M. J., & Clark, T. L. (2001). Numerical modeling of gravity wave generation by deep tropical convection. *Journal of the Atmospheric Sciences*, *58*(10), 1249–1274. https://doi.org/10.1175/1520-0469(2001)058⟨1249:NMOGWG⟩2.0.CO;2

Lane, T. P., Reeder, M. J., & Guest, F. M. (2003). Convectively generated gravity waves observed from radiosonde data taken during MCTEX. *Quarterly Journal of the Royal Meteorological Society*, *129*(590), 1731–1740. https://doi.org/10.1256/qj.02.196

Leblanc, T., & Hauchecorne, A. (1997). Recent observations of mesospheric temperature inversions. *Journal of Geophysical Research*, *102*(D16), 19471–19482. https://doi.org/10.1029/97JD01445

Lighthill, M. (1978). *Waves in fluids*. Cambridge University Press. Retrieved from https://books.google.com.br/books?id=oVXTngEACAAJ

Liu, A. Z., & Swenson, G. R. (2003). A modeling study of O_2 and OH airglow perturbations induced by atmospheric gravity waves. *Journal of Geophysical Research*, *108*(D4), 4151. https://doi.org/10.1029/2002JD002474

Medeiros, A. F., Fechine, J., Buriti, R. A., Takahashi, H., Wrasse, C. M., & Gobbi, D. (2005). Response of OH, O_2 and OI5577 airglow emissions to the mesospheric bore in the equatorial region of Brazil. *Advances in Space Research*, *35*(11), 1971–1975. https://doi.org/10.1016/j.asr.2005.03.075

Modeling, G., & (GMAO), A. O. (2015). Merra-2 inst3_3d_asm_np: 3d, 3-hourly, instantaneous, pressure-level, assimilation, assimilated meteorological fields v5. 12.4. GES DISC, [dataset]. https://doi.org/10.5067/WWQSXQ8IVFW8

Nappo, C. J. (2013). *An introduction to atmospheric gravity waves*. Academic Press.

NOAA. (2019). Cape for instability descriptors. Retrieved from noaa.gov/misc/tables/capetext.htm

Nyassor, P. K., Buriti, R. A., Paulino, I., Medeiros, A. F., Takahashi, H., Wrasse, C. M., & Gobbi, D. (2018). Determination of gravity wave parameters in the airglow combining photometer and imager data. *Annales Geophysicae*, *36*(3), 705–715. https://doi.org/10.5194/angeo-36-705-2018

Nyassor, P. K., Wrasse, C. M., Gobbi, D., Paulino, I., Vadas, S. L., Naccarato, K. P., et al. (2021). Case studies on concentric gravity waves source using lightning flash rate, brightness temperature and backward ray tracing at São Martinho da Serra (29.44°s, 53.82°w). *Journal of Geophysical Research: Atmospheres*, *126*(10), e2020JD034527. https://doi.org/10.1029/2020JD034527

Paulino, I., Figueiredo, C. A., Rodrigues, F., Buriti, R. A., Wrasse, C. M., Paulino, A. R., et al. (2020). Atmospheric gravity waves observed in the nightglow following the 21 August 2017 total solar eclipse. *Geophysical Research Letters*, *47*(17), e2020GL088924. https://doi.org/10.1029/2020GL088924

Paulino, I., Takahashi, H., Vadas, S. L., Wrasse, C. M., Sobral, J., Medeiros, A., et al. (2012). Forward ray-tracing for medium-scale gravity waves observed during the COPEX campaign. *Journal of Atmospheric and Solar-Terrestrial Physics*, *90*, 117–123. https://doi.org/10.1016/j.jastp.2012.08.006

Pedoe, D. (1995). *Circles: A mathematical view*. Cambridge University Press.

Perwitasari, S., Sakanoi, T., Nakamura, T., Ejiri, M., Tsutsumi, M., Tomikawa, Y., et al. (2016). Three years of concentric gravity wave variability in the mesopause as observed by IMAP/VISI. *Geophysical Research Letters*, *43*(22), 11–528. https://doi.org/10.1002/2016GL071511

Picone, J., Hedin, A., Drob, D. P., & Aikin, A. (2002). Nrlmsise-00 empirical model of the atmosphere: Statistical comparisons and scientific issues. *Journal of Geophysical Research*, *107*(A12), SIA15-1–SIA15-16. https://doi.org/10.1029/2002JA009430

Press, W. H., Teukolsky, S. A., Vetterling, W. T., & Flannery, B. P. (2007). Numerical recipes. In *The art of scientific computing* (3rd ed.). Cambridge University Press.

Rozante, J. R., Gutierrez, E. R., Fernandes, A. d. A., & Vila, D. A. (2020). Performance of precipitation products obtained from combinations of satellite and surface observations. *International Journal of Remote Sensing*, *41*(19), 7585–7604. https://doi.org/10.1080/01431161.2020.1763504

Rozante, J. R., Moreira, D. S., de Goncalves, L. G. G., & Vila, D. A. (2010). Combining TRMM and surface observations of precipitation: Technique and validation over South America. *Weather and Forecasting*, *25*(3), 885–894. https://doi.org/10.1175/2010WAF2222325.1

Sentman, D., Wescott, E., Picard, R., Winick, J., Stenbaek-Nielsen, H., Dewan, E., et al. (2003). Simultaneous observations of mesospheric gravity waves and sprites generated by a midwestern thunderstorm. *Journal of Atmospheric and Solar-Terrestrial Physics*, *65*(5), 537–550. https://doi.org/10.1016/S1364-6826(02)00328-0

Simkhada, D., Snively, J., Taylor, M. J., & Franke, S. (2009). Analysis and modeling of ducted and evanescent gravity waves observed in the Hawaiian airglow. *Annales Geophysicae*, *27*(8), 3213–3224. https://doi.org/10.5194/angeo-27-3213-2009

Snively, J. B., Pasko, V. P., Taylor, M. J., & Hocking, W. K. (2007). Doppler ducting of short-period gravity waves by midlatitude tidal wind structure. *Journal of Geophysical Research*, *112*(A3), A03304. https://doi.org/10.1029/2006JA011895

Suzuki, S., Shiokawa, K., Otsuka, Y., Ogawa, T., Nakamura, K., & Nakamura, T. (2007). A concentric gravity wave structure in the mesospheric airglow images. *Journal of Geophysical Research*, *112*(D2), D02102. https://doi.org/10.1029/2005JD006558

Suzuki, S., Vadas, S. L., Shiokawa, K., Otsuka, Y., Kawamura, S., & Murayama, Y. (2013). Typhoon-induced concentric airglow structures in the mesopause region. *Geophysical Research Letters*, *40*(22), 5983–5987. https://doi.org/10.1002/2013GL058087

Tsuda, T. (2014). Characteristics of atmospheric gravity waves observed using the mu (middle and upper atmosphere) radar and GPS (global positioning system) radio occultation. *Proceedings of the Japan Academy, Series B*, *90*(1), 12–27. https://doi.org/10.2183/pjab.90.12

Utida, G., Cruz, F. W., Etourneau, J., Bouloubassi, I., Schefuß, E., Vuille, M., et al. (2019). Tropical south Atlantic influence on northeastern Brazil precipitation and itcz displacement during the past 2300 years. *Scientific Reports*, *9*(1), 1–8. https://doi.org/10.1038/s41598-018-38003-6

Vadas, S. L. (2007). Horizontal and vertical propagation and dissipation of gravity waves in the thermosphere from lower atmospheric and thermospheric sources. *Journal of Geophysical Research*, *112*(A6), A06305. https://doi.org/10.1029/2006JA011845

Vadas, S. L., & Azeem, I. (2020). Concentric secondary gravity waves in the thermosphere and ionosphere over the continental United States on 25-26 march 2015 from deep convection. *Journal of Geophysical Research: Space Physics*, e2020JA028275. https://doi.org/10.1029/2020JA028275

Vadas, S. L., & Becker, E. (2019). Numerical modeling of the generation of tertiary gravity waves in the mesosphere and thermosphere during strong mountain wave events over the southern Andes. *Journal of Geophysical Research: Space Physics*, *124*(9), 7687–7718. https://doi.org/10.1029/2019JA026693

Vadas, S. L., & Crowley, G. (2010). Sources of the traveling ionospheric disturbances observed by the ionospheric TIDDBIT sounder near Wallops Island on 30 October 2007. *Journal of Geophysical Research*, *115*(A7), A07324. https://doi.org/10.1029/2009JA015053

Vadas, S. L., & Fritts, D. (2009). Reconstruction of the gravity wave field from convective plumes via ray tracing. *Annales Geophysicae: Atmospheres, Hydrospheres and Space Sciences*, *27*(1), 147–177. https://doi.org/10.5194/angeo-27-147-2009

Vadas, S. L., & Fritts, D. C. (2001). Gravity wave radiation and mean responses to local body forces in the atmosphere. *Journal of the Atmospheric Sciences*, *58*(16), 2249–2279. https://doi.org/10.1175/1520-0469(2001)058⟨2249:GWRAMR⟩2.0.CO;2

Vadas, S. L., & Fritts, D. C. (2005). Thermospheric responses to gravity waves: Influences of increasing viscosity and thermal diffusivity. *Journal of Geophysical Research*, *110*(D15), D15103. https://doi.org/10.1029/2004JD005574

Vadas, S. L., & Fritts, D. C. (2006). Influence of solar variability on gravity wave structure and dissipation in the thermosphere from tropospheric convection. *Journal of Geophysical Research*, *111*(A10), A10S12. https://doi.org/10.1029/2005JA011510

Vadas, S. L., Fritts, D. C., & Alexander, M. J. (2003). Mechanism for the generation of secondary waves in wave breaking regions. *Journal of the Atmospheric Sciences*, *60*(1), 194–214. https://doi.org/10.1175/1520-0469(2003)060⟨0194:MFTGOS⟩2.0.CO;2

Vadas, S. L., & Liu, H.-l. (2009). Generation of large-scale gravity waves and neutral winds in the thermosphere from the dissipation of convectively generated gravity waves. *Journal of Geophysical Research*, *114*(A10), A10310. https://doi.org/10.1029/2009JA014108

Vadas, S. L., Taylor, M. J., Pautet, P.-D., Stamus, P., Fritts, D. C., Liu, H.-L., et al. (2009). Convection: The likely source of the medium-scale gravity waves observed in the OH airglow layer near Brasilia, Brazil, during the SpreadFEX campaign. *Annales Geophysicae*, *27*(1), 231–259. https://doi.org/10.5194/angeo-27-231-2009

Vadas, S. L., Yue, J., & Nakamura, T. (2012). Mesospheric concentric gravity waves generated by multiple convective storms over the North American great plain. *Journal of Geophysical Research*, *117*(D7),D07113. https://doi.org/10.1029/2011JD017025

Vadas, S. L., Yue, J., She, C.-Y., Stamus, P. A., & Liu, A. Z. (2009). A model study of the effects of winds on concentric rings of gravity waves from a convective plume near Fort Collins on 11 may 2004. *Journal of Geophysical Research*, *114*(D6), D06103. https://doi.org/10.1029/2008JD010753

Vadas, S. L., Zhao, J., Chu, X., & Becker, E. (2018). The excitation of secondary gravity waves from local body forces: Theory and observation. *Journal of Geophysical Research: Atmospheres*, *123*(17), 9296–9325. https://doi.org/10.1029/2017JD027970

Vargas, F., Swenson, G., Liu, A., & Pautet, D. (2016). Evidence of the excitation of a ring-like gravity wave in the mesosphere over the Andes Lidar observatory. *Journal of Geophysical Research: Atmospheres*, *121*(15), 8896–8912. https://doi.org/10.1002/2016JD024799

Wrasse, C. M., Nakamura, T., Tsuda, T., Takahashi, H., Gobbi, D., Medeiros, A. F., & Taylor, M. J. (2003). Atmospheric wind effects on the gravity wave propagation observed at 22.7°s-Brazil. *Advances in Space Research*, *32*(5), 819–824. https://doi.org/10.1016/S0273-1177(03)00413-7

Wrasse, C. M., Takahashi, H., Medeiros, A. F., Lima, L. M., Taylor, M. J., Gobbi, D., & Fechine, J. (2007). Determinaçao dos parâmetros de ondas de gravidade através da análise espectral de imagens de aeroluminescência. *Revista Brasileira de Geofísica*, *25*(3), 257–265. https://doi.org/10.1590/S0102-261X2007000300003

Xu, J., Li, Q., Yue, J., Hoffmann, L., Straka, W. C., Wang, C., et al. (2015). Concentric gravity waves over northern China observed by an airglow imager network and satellites. *Journal of Geophysical Research: Atmospheres*, *120*(21), 11058–11078. https://doi.org/10.1002/2015JD023786

Yiğit, E., Aylward, A. D., & Medvedev, A. S. (2008). Parameterization of the effects of vertically propagating gravity waves for thermosphere general circulation models: Sensitivity study. *Journal of Geophysical Research*, *113*(D19), D19106. https://doi.org/10.1029/2008JD010135

Yiğit, E., & Medvedev, A. S. (2015). Internal wave coupling processes in Earth's atmosphere. *Advances in Space Research*, *55*(4), 983–1003. https://doi.org/10.1016/j.asr.2014.11.020

Yiğit, E., Medvedev, A. S., Aylward, A. D., Hartogh, P., & Harris, M. J. (2009). Modeling the effects of gravity wave momentum deposition on the general circulation above the turbopause. *Journal of Geophysical Research*, *114*(D7), D07101. https://doi.org/10.1029/2008JD011132

Yiğit, E., Medvedev, A. S., & Ern, M. (2021). Effects of latitude-dependent gravity wave source variations on the middle and upper atmosphere. *Frontiers in Astronomy and Space Sciences*, *7*. https://doi.org/10.3389/fspas.2020.614018

Yue, J., Hoffmann, L., & Joan Alexander, M. J. (2013). Simultaneous observations of convective gravity waves from a ground-based airglow imager and the airs satellite experiment. *Journal of Geophysical Research: Atmospheres*, *118*(8), 3178–3191. https://doi.org/10.1002/jgrd.50341

Yue, J., Vadas, S. L., She, C.-Y., Nakamura, T., Reising, S. C., Liu, H.-L., et al. (2009). Concentric gravity waves in the mesosphere generated by deep convective plumes in the lower atmosphere near fort Collins, Colorado. *Journal of Geophysical Research*, *114*(D6), D06104. https://doi.org/10.1029/2008JD011244